crystals

MDPI

Article

Effect of Pore Defects on Very High Cycle Fatigue Behavior of TC21 Titanium Alloy Additively Manufactured by Electron Beam Melting

Qingdong Li [1], Shuai Liu [1], Binbin Liao [1], Baohua Nie [1,*], Binqing Shi [1], Haiying Qi [1], Dongchu Chen [2,*] and Fangjun Liu [3,*]

1 School of Materials Science and Hydrogen Energy, Foshan University, Foshan 528000, China
2 Guangdong Key Laboratory for Hydrogen Energy Technologies, Foshan 528000, China
3 School of Mechatronic Engineering and Automation, Foshan University, Foshan 528000, China
* Correspondence: niebaohua@fosu.edu.cn (B.N.); chendc@fosu.edu.cn (D.C.); liufj@fosu.edu.cn (F.L.); Tel.: +86-075782700525 (B.N.); +86-075782700525 (D.C.); +86-075782700817 (F.L.)

Abstract: Titanium alloys additively manufactured by electron beam melting (EBM) inevitably obtained some pore defects, which significantly reduced the very high cycle fatigue performance. An ultrasonic fatigue test was carried out on an EBM TC21 titanium alloy with hot isostatic pressing (HIP) and non-HIP treatment, and the effect of pore defects on the very high cycle fatigue (VHCF) behavior were investigated for the EBM TC21 titanium alloy. The results showed that the S-N curve of non-HIP specimens clearly had a tendency to decrease in very high cycle regimes, and HIP treatment significantly improved fatigue properties. Fatigue limits increased from 250 MPa for non-HIP specimens to 430 MPa for HIP ones. Very high cycle fatigue crack mainly initiated from the internal pore for EBM specimens, and a fine granular area (FGA) was observed at the crack initiation site in a very high cycle regime for both non-HIP and HIP specimens. ΔK_{FGA} had a constant trend in the range from 2.7 MPa$\sqrt{m}$ to 3.5 MPa$\sqrt{m}$, corresponding to the threshold stress intensity factor range for stable crack propagation. The effect of pore defects on the very high cycle fatigue limit was investigated based on the Murakami model. Furthermore, a fatigue indicator parameter (FIP) model based on pore defects was established to predict fatigue life for non-HIP and HIP specimens, which agreed with the experimental data.

Keywords: titanium alloy; EBM; VHCF; HIP; pore defects

Citation: Li, Q.; Liu, S.; Liao, B.; Nie, B.; Shi, B.; Qi, H.; Chen, D.; Liu, F. Effect of Pore Defects on Very High Cycle Fatigue Behavior of TC21 Titanium Alloy Additively Manufactured by Electron Beam Melting. *Crystals* **2023**, *13*, 1327. https://doi.org/10.3390/cryst13091327

Academic Editors: Wangzhong Mu and Chao Chen

Received: 12 August 2023
Revised: 28 August 2023
Accepted: 28 August 2023
Published: 30 August 2023

1. Introduction

Titanium alloys were widely used in aerospace due to their high specific strength and excellent corrosion resistance [1]. The components fabricated by additive manufacturing (AM) were more efficient, had shorter cycles, and free structural design [2–4]. Compared with selective laser melting (SLM), the EBM titanium alloy underwent a special thermal history due to the influence of high preheating temperature, resulting in an $\alpha + \beta$ dual-phase microstructure and low residual stress [5]. Fatigue fracture of these EBM titanium alloy components in aerospace still occurred when subjected to high frequency and low-stress cyclic loads during ultra-long life service (>10^7 cycles), i.e., VHCF, where fatigue cracks initiated from the specimen interior, and FGA was observed at the crack initiation site [6,7]. Therefore, the VHCF performance of titanium alloy components fabricated by EBM was a key factor for large-scale applications.

The widespread application of AM components was limited due to their inherent defects, such as pores, lack of fusion (LoF), and mirocracks. Fatigue properties of EBM titanium alloy components were still lower than that of the forgings ones, owing to the promotion of crack initiation by defects [8,9]. The Murakami model was widely used to evaluate the relationship between fatigue strength and defects in AM components [10].

The fatigue scatter and size effect of AM materials with defects were investigated based on the extreme value statistics theory and probability fatigue theory [11]. Furthermore, based on the weakest-link theory, a probability fatigue life model was established to analyze the location and size effects of defects [12]. The FIP model based on the stress intensity factor of defects had been applied to predict fatigue life for the titanium alloy [13].

In a very high cycle regime, fatigue crack initiation and fatigue life were much more sensitive to the defects in AM titanium alloys. The investigation by Günther [14] showed that very high cycle fatigue cracks initiated from pores and LoF for EBM titanium alloy, where FGA characteristics were observed around these defects. Fatigue performance was similar to that of the SLM specimens after stress-release treatment, indicating that the EBM specimens did not require stress-relieving annealing due to their low residual stress [8]. However, much research on very high cycle fatigue was focused on SLM titanium alloys [15–17]. The internal defects (pores, lack of fusion, etc.) and surface artificial defects dramatically reduced the very high cycle fatigue properties of the SLM titanium alloy, and fatigue strength models based on defect size were proposed based on the Murakami model [18].

HIP was widely applied to improve fatigue performance due to the reduction of defects in EBM titanium alloy components [19]. However, little attention was paid to the very high cycle fatigue behavior of the EBM titanium alloy treated by HIP. As for SLM titanium alloys, HIP significantly improved the very high cycle fatigue performance, which can be comparable to that of conventional forged ones, although HIP treatment coarsened the microstructure and reduced the tensile strength of the SLM Ti6Al4V titanium alloy [18,20]. A very high cycle fatigue crack initiated at the large α phase of SLM Ti6Al4V alloy was treated by HIP [14], suggesting that the reduction of the α phase size after HIP treatment can further improve very high cycle fatigue performance. Furthermore, it should be noted that the combination of HIP and surface machining can effectively enhance the fatigue performance of EBM titanium alloy components. HIP treatment did not generally improve the fatigue life of the AM titanium alloy without machining on the surface due to the effect of the surface roughness [9], while the specimens obtained excellent fatigue properties after HIP treatment and surface machining.

The very high cycle fatigue behavior of the EBM TC21 titanium alloy, which was developed for aerospace structural components, was investigated. Considering that LoF had a more negative impact on fatigue performance than pore defects [21], the EBM process with high energy input and low forming rate was adopted to restrain the dangerous LoF defects. Then, the effect of the internal pore in the EBM titanium alloy on very high cycle fatigue properties and the crack-initiation mechanism was discussed in comparison with that of HIP ones. Very high cycle fatigue strength and fatigue life of an EBM titanium alloy containing internal pore defects were quantitatively evaluated based on the Murakami model and FIP model, which was beneficial for the application of EBM titanium alloy components in aerospace engineering.

2. Experimental Procedures

2.1. Materials and Manufacturing

The TC21 titanium alloy was manufactured by EBM on an Arcam A2 machine (Arcam, Stockholm, Sweden) under a 5×10^{-3} Pa vacuum. The chemical composition (wt.%) of the powder is shown in Table 1. The diameter size of the particle was in the range of 50 to 125 µm. Preheating the chamber at 650 °C reduced the residual stress during EBM. To avoid the formation of dangerous LoF defects, an EBM process with high energy input and low forming rate was adopted to promote powder melting. EBM fabrication was operated at a voltage of 60 kV, beam current of 30 mA, spot size of 300 µm, and each layer thickness of 50 µm.

Table 1. Chemical composition of TC21 powder.

Al	Zr	Mo	Cr	Nb	Sn	O	H	Ti
6.26	2.13	2.38	0.96	1.84	1.87	0.092	0.0043	Bal.

The parts on the substrate were a length of 180 mm, height of 100 mm, and width of 15 mm. Fatigue specimens were cut from the building parts, and their longitudinal axis was parallel to the build direction. In order to eliminate the pore defects, HIP for EBM specimens were treated by a QIH-15 machine (ABB company, Vsters, Sweden) at 920 °C under 1000 bar for 2 h, and then the specimens were cooled using nitrogen gas.

Hardness measurements were carried out by a FM310 (Future-Tech, Tokyo, Japan) machine for both HIP and non-HIP specimens. Hardness values were obtained from five tests under a load of 0.5 kg for 15 s.

2.2. Ultrasonic Fatigue Test

Fatigue tests were carried out using a USF-2000 ultrasonic fatigue test machine (Shimadzu, Kyoto, Japan) with R = −1 and a frequency of 20 kHz [22]. The investigation [23] indicated that the frequency had little influence on ultrasonic fatigue tests under low-stress amplitude. Detailed information about the ultrasonic fatigue test machine was present in the reference [24]. To control the thermal effects of high-frequency fatigue tests, compressed air was used to cool the specimens.

Based on the elastic wave theory, the specimen was designed to work at resonance with the amplifier, and the geometries of the fatigue specimens are shown in Figure 1. According to Figure 1, the ultrasonic fatigue specimens were processed from the EBM parts. Thus, the rough surface of the EBM parts was removed by mechanical processing.

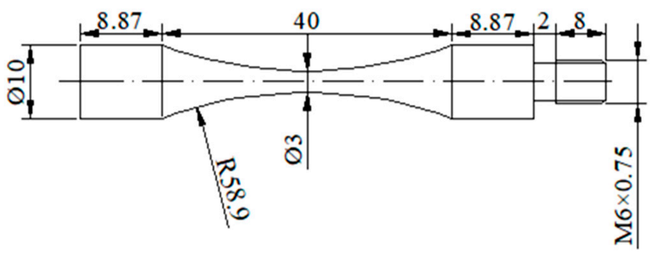

Figure 1. Shape and size of ultrasonic fatigue specimens.

Electro-polishing was treated on fatigue specimens to eliminate the machining influence on fatigue behavior. The electro-polishing process was under −20 °C and 20–25 V with 59% methanol, 35% n-butanol, and 6% perchloric acid. The fracture surfaces and microstructure were observed by CS3400 scanning electron microscopy (CamScan, Cambs, UK).

3. Results

3.1. VHCF Properties

Figure 2 shows the microstructure of the EBM TC21 alloy with non-HIP and HIP treatment, respectively. The microstructure for non-HIP treatment was basketweaved with a lamellar α phase, whereas the HIP treatment increased the size of the α phase. The mean hardness for non-HIP and HIP samples was 435 HV and 418 HV, respectively.

S-N curves of the EBM TC21 titanium alloy with the non-HIP and HIP treatment are shown in Figure 3. It showed that the curve of non-HIP specimens displayed a continuously descending characteristic, and fatigue life gradually increased with the decrease of fatigue stress. As the stress amplitude decreased, fatigue crack initiation characteristics changed from surface initiation to interior pore initiation without FGA and interior pore initiation with FGA. When the fatigue life exceeds 2×10^6 cycles, FGA characteristics can be observed around the pores at the fatigue crack initiation site. If the specimens did not break at

10^9 cycles, the stress amplitude can be defined as the very high cycle fatigue limit. Thus, EBM TC21 titanium alloy obtained a very high cycle fatigue limit of 250 MPa. Very high cycle fatigue S-N curve characteristics and fatigue limit of the EBM TC21 alloy were similar to that of EBM Ti6Al4V [14], but the fatigue limit was far lower than that of forged ones with a basketweave microstructure [25].

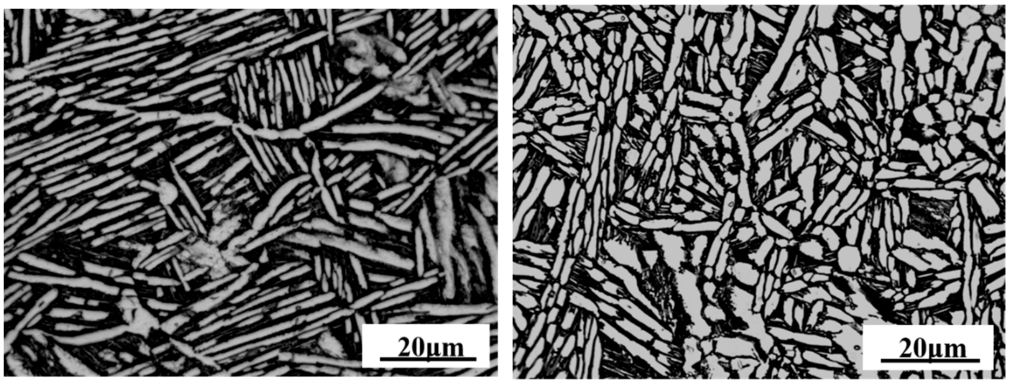

(**a**) (**b**)

Figure 2. Microstructure of EBM titanium alloy: (**a**) non-HIP; (**b**) HIP.

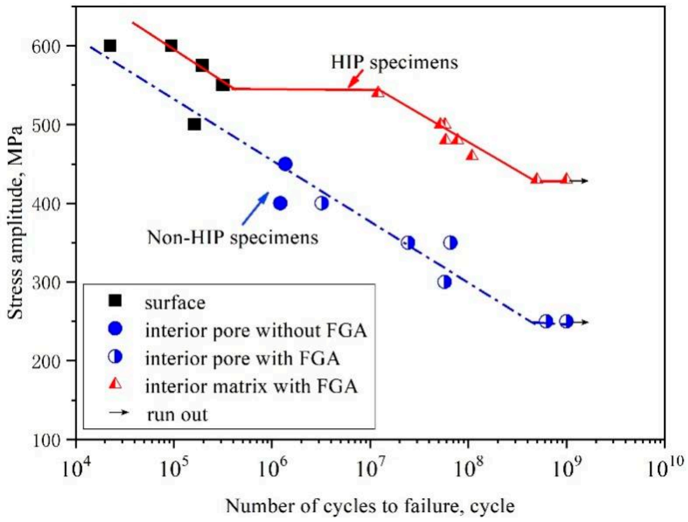

Figure 3. S-N curves for the non-HIP and HIP specimens.

Figure 3 also illustrated that HIP treatment dramatically improved fatigue properties in comparison with the non-HIP condition. The HIP specimens obtained a higher fatigue life at the same cyclic stress. It displayed a two-step curve for the HIP specimens, which was similar to that of the forged ones [25]. The VHCF limit was increased from 250 MPa for the HIP specimens to 430 MPa for the non-HIP ones. There was a transition platform from crack surface initiation under high stress to internal initiation under a 550 MPa stress amplitude. The fatigue life of surface-initiated cracks was lower than that of internally initiated cracks due to the environmental and stress concentration factors. However, the non-HIP specimens exhibited a continuous decease feature due to the presence of defects.

3.2. Fractograph

For EBM materials, insufficient energy input resulted in incomplete melting of the powder and LoF, whereas excessive energy input led to an unstable molten pool and vaporization, forming pore defects. As for the non-HIP specimens, the pore defects had a significant impact on the fatigue crack initiation characteristics for the EBM TC21 titanium alloy. Figure 4a shows that under 600 MPa stress amplitude, a crack initiated from the specimen surface without pore defects at the initiation site, as indicated by the red arrow.

When the stress amplitude decreased to 450 MPa, fatigue cracks initiated at a large pore inside the specimen (Figure 4b), where stage I propagation along the facet was observed near the pore. Under lower stress amplitude, fatigue cracks initiated at a small pore inside the specimen, and a fish-eye characteristic and FGA were observed near the pore (Figure 4c), which was a typical characteristic of VHCF of titanium alloys [6,7] and were consistent with that of the EBM Ti6Al4V alloy and SLM Ti6Al4V in the investigation by Günther [14]. It should be noted that even if the equivalent diameter of small pores in the EBM TC21 titanium alloy decreased to 12 μm, these small pores still promoted the VHCF crack initiation, and there were FGA characteristics around the pores (Figure 4d).

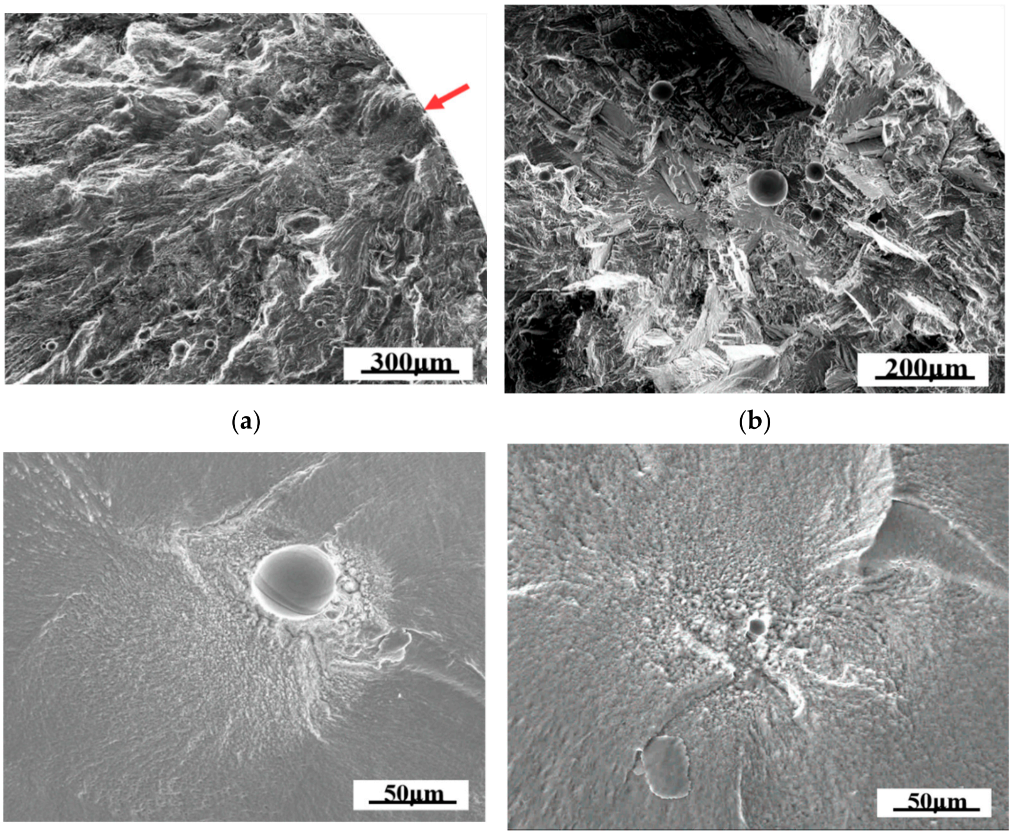

(**a**) (**b**) (**c**) (**d**)

Figure 4. Fracture surface of non-HIP specimens: (**a**) σ_a = 600 MPa and Nf = 2.22 × 10^4 cycles; (**b**) σ_a = 450 MPa and Nf = 1.37 × 10^6 cycles; (**c**) σ_a = 300 MPa and N_f = 5.75 × 10^7 cycles; (**d**) σ_a = 250 MPa and N_f = 6.2 × 10^8 cycles. (Red arrow denoted the initiation site of surface crack).

As for the HIP specimens, the pores in EBM specimens were eliminated by HIP treatment. Under low stress, cracks initiated at the inner of the HIP specimen in the long-life regime, as indicated by the red ring (Figure 5a). An FGA characteristic without pore defects was present at the crack initiation site (Figure 5b), which was similar to the forged TC21 titanium alloy [25] and SLM Ti6Al4V alloy after HIP treatment [18,20]. In comparison, the investigation by Günther [14] suggested that VHCF cracks initiated at the large α phase of the SLM Ti6Al4V alloy treated by HIP with faceted fracture characteristics, which was attributed to the difference in microstructure.

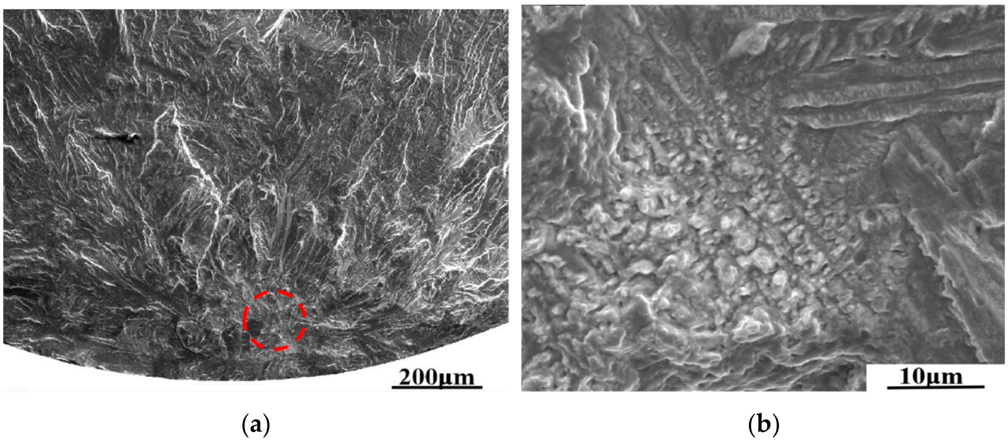

Figure 5. Fracture surface of HIP specimens at σ_a = 460 MPa and $N_f = 1.09 \times 10^8$ cycles. (**a**) Crack initiation site, (**b**) FGA characteristic at crack initiation site. (Red ring denoted the initiation site of internal crack).

4. Discussion

4.1. Effect of Defect on Fracture Mechanism

Under high-stress amplitude, small pore defects were irrelevant to fatigue crack initiation, and the non-HIP specimens exhibited the surface crack initiation behavior (Figure 4a), and the slip band activity resulted in crack initiation. Fatigue crack initiated at the pore inside the specimens under low-stress amplitude. Stage I propagation along the facet was presented around the large pore under a 450 MPa stress amplitude (Figure 4b), while FGA was observed around the pore under a lower stress amplitude (Figure 4c,d). Figure 6 showed that the areas of the pore ranged from 100 μm^2 to 3840 μm^2, and there was no direct relationship between the area of the pore and fatigue life N_f. However, the area of FGA increased with fatigue life N_f. As FGA was formed by the discontinuous propagation of microcracks [6], it indicated that the consumption life in FGA was a major part of fatigue life.

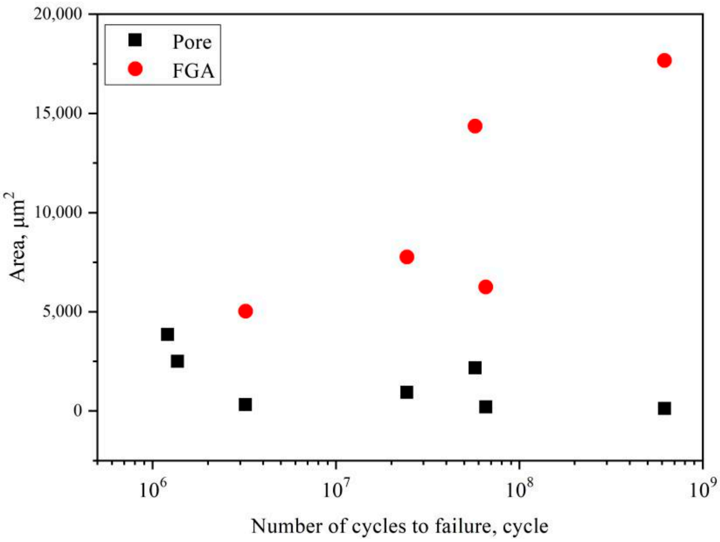

Figure 6. Relationship between the size of pore and fatigue life for EBM titanium alloy.

The stress intensity factor range ΔK_{pore} at the front of the pore inside the specimens can be expressed as [10]:

$$\Delta K_{pore} = 0.5\sigma_a \sqrt{\pi \sqrt{area_{pore}}} \quad (1)$$

where σ_a is the stress amplitude and $area_{pore}$ is the area of the pore at the crack initiation site. As for FGA, ΔK_{FGA} can be calculated by substituting $area_{FGA}$ into Equation (1).

Figure 7 shows that ΔK_{pore} was not directly related to fatigue life due to the random distribution of pore size but displayed a decreased trend. Similar to cast alloys, there exists the critical stress intensity factor K_{cr} with pores [26], and the value of K_{cr} for EBM TC21 titanium alloy was 0.78 MPa$\sqrt{\text{m}}$ in a very high cycle regime. The pore size was small enough, especially for HIP treatment, where K_{pore} was lower than K_{cr}; thus, the pore had no decisive effect on the cracks' initiation and fatigue cracks initiated from microstructure inhomogeneity for EBM specimens treated by HIP treatment (Figure 5).

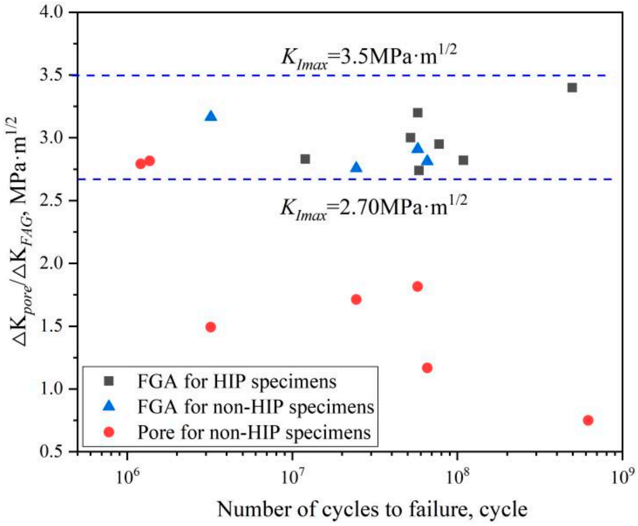

Figure 7. Relationship ΔK_{pore}, ΔK_{FGA} with fatigue life.

Furthermore, Figure 7 also shows that ΔK_{FGA} was independent of fatigue life from 10^6 cycles to 10^9 cycles and had a constant trend in the range from 2.7 MPa$\sqrt{\text{m}}$ to 3.5 MPa$\sqrt{\text{m}}$, which was considered as the stable crack growth threshold ΔK_{th} for titanium alloys [20,27]. The stable crack growth ΔK_{th} for forged the TC21 titanium alloy ranged from 3.8 MPa$\sqrt{\text{m}}$ to 4.5 MPa$\sqrt{\text{m}}$ [25]. The value of ΔK_{FGA} for the EBM TC21 titanium alloy was lower than that of the forged ones.

As for non-HIP specimens with 400 MPa/1.37 $\times$ 10^6 cycles and 450 MPa/1.26 $\times$ 10^6 cycles, the value of ΔK_{pore} reached that of ΔK_{FGA}, and fatigue cracks, which originated from these pores, could continuously propagate to failure. Therefore, the FGA was not observed around the pores for these two specimens. When ΔK_{pore} is lower than ΔK_{FGA}, fatigue cracks cannot propagate continuously, resulting in FGA. For the non-HIP specimen with 300 MPa/5.7 $\times$ 10^7 cycles, the equivalent diameter of FGA was approximately 105 µm, and the average propagation rate was 8.77 $\times$ 10^{-13} m/cycle, which was much lower than the Burgers vector. Thus, microcracks discontinuously propagated within FGA.

VHCF cracks initiated from the heterogeneous microstructure in the HIP specimens (Figure 5). Many models, such as numerous cyclic pressing (NCP) [28] and FGA [29], were established to reveal the FGA formation. A heterogeneous cyclic strain concentration occurred at the α/β interface due to the highly inhomogeneous dislocation arrangement [30]. A nanocrystalline layer was formed at the stress concentration area under very high cyclic loading, and the nanocrystalline boundaries were separated to form fine-grain characteristics [28,29].

4.2. Effect of Defect on Fatigue Strength

To quantitatively analyze the fatigue strength of the EBM titanium alloy with pore defects, the maximum pore size on the fracture surface was estimated by the statistical extreme value method. The pore sizes were assumed to follow the Gumbel distribution [31], and the pore size of EBM titanium alloys was plotted using the Gumbel extreme value analysis. In Figure 8, i/(N + 1) was the cumulative probability corresponding to the maximum pore size in each field of view and arranged in descending order. The maximum pore diameter of the EBM titanium alloy was evaluated as 96.2 μm.

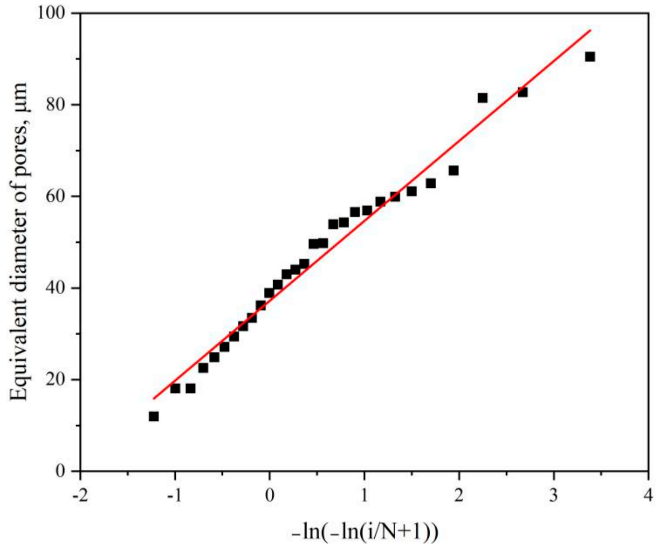

Figure 8. Statistics of pore diameter in additive manufacturing.

For EBM titanium alloys with internal defects, fatigue strength can be evaluated using the Murakami model [14]:

$$\sigma_w = \frac{1.56 \times (HV + 120)}{\left(\sqrt{area_{pore}}\right)^{1/6}} \tag{2}$$

The parameter $area_{pore}$ was considered as the equivalent area of pores perpendicular to the direction of stress loading. Vickers hardness (HV) was the hardness of the material. The location parameter 1.56 was applicable to the internal defects.

Based on Equation (2), fatigue strengths of the EBM titanium alloy were 197 MPa, 230 MPa, and 394 MPa, respectively, corresponding to the maximum pore diameter of 96.2 μm, the average diameter of 60 μm, and the minimum diameter of 12 μm. The maximum size of the pore defect evaluated by the statistical extreme value method corresponded to the lowest limit of fatigue strength of the EBM titanium alloy. Compared with Figure 3, fatigue strength with the average pore size relatively approached the experimental data with an error of 8%. Fatigue strength corresponding to the minimum pore defect was much higher than the experimental data, while it was closer to the fatigue strength of the EBM titanium alloy after HIP treatment. It revealed that HIP reduced the pore size, thereby improving the fatigue strength of the EBM titanium alloy.

4.3. Effect of Defect on Fatigue Life

As mentioned above, the porosity defects significantly reduced the very high cycle fatigue life of the AM titanium alloy, and the defect factor should be considered for the fatigue life predicting model. The *FIP* model revealed the promoting effect of material defects and cyclic stress on fatigue damage and can be calculated as [26]:

$$FIP = \frac{\mu \sigma_a}{E}\left[1 + k\frac{\Delta K_{defect}}{\Delta K_{th}}\right] \tag{3}$$

where Schmid factor μ was equal to 0.408, and parameter k was equal to 1 [26]. ΔK_{defect} was estimated by Equation (1), and ΔK_{defect} was considered as the mean value of ΔK_{FGA}. As for HIP specimens, the pore defects were eliminated, and the K_{defect} was equal to zero.

The fatigue life was numerically fitted with *FIP* parameters based on fatigue data of non-HIP and HIP specimens, and the expression was

$$N_f = 7.86 \times 10^{-19}(FIP)^{-9.46} \tag{4}$$

The fitting curve between *FIP* parameters and fatigue life is shown in Figure 9. It showed that the prediction of fatigue life based on Equation (4) agreed well with the experimental data. The HIP specimens had a lower value of FIP and higher fatigue life than those of the non-HIP ones.

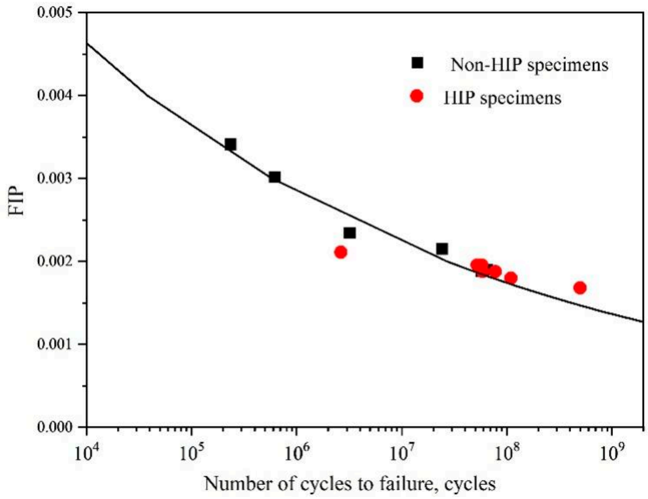

Figure 9. *FIP* versus the number of cycles to failure.

Based on the *FIP* model, the prediction of S-N curves for both non-HIP and HIP specimens is shown in Figure 10. The average diameter of the pores was calculated as 60 µm, and the prediction of fatigue life generally agreed with the experimental data. Obviously, EBM titanium alloys with a smaller defect obtained a longer fatigue life at the same stress level. For HIP treatment, pores in EBM titanium alloy specimens were considered to be healed with a diameter of zero. HIP treatment significantly improved fatigue life owing to the elimination of pore defects. Thus, the fatigue life of EBM titanium alloys with pore defects can be well predicted based on the FIP model.

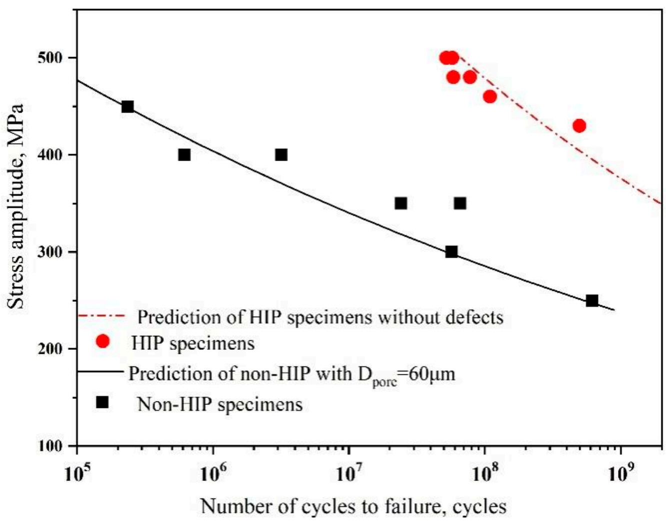

Figure 10. Prediction of fatigue life for the EBM TC21 titanium alloy based on the *FIP* model.

5. Conclusions

The VHCF of the EBM TC21 titanium alloy with HIP and non-HIP treatment was carried out by ultrasonic fatigue test, and the effect of pore defects on VHCF behavior was investigated based on the Murakami model and FIP model for the EBM TC21 titanium alloy. The conclusions are summarized as follows:

(1) The curve of the EBM TC21 titanium alloy displayed a continuously descending characteristic in a very high cycle regime, while HIP treatment significantly improved fatigue properties and illustrated two-step curve characteristics similar to the forged ones;
(2) The VHCF cracks were mainly initiated from the internal pore of the EBM TC21 titanium alloy, whereas cracks were initiated at the inner heterogeneous microstructure for HIP specimens in the very high cycle regime. FGA was observed at the crack initiation site in a very high cycle regime for both non-HIP and HIP specimens. The value of ΔK_{FGA} corresponded with the threshold of stable crack propagation;
(3) Based on the Murakami model, the lower limit of fatigue strength for the EBM TC21 titanium alloy was estimated by the statistical extreme value method. Fatigue strength with the average pore size relatively approached the experimental data with an error of 8%. Furthermore, a *FIP* model based on material defects was established to predict fatigue life for non-HIP and HIP specimens, which agreed well with the experimental data.

Author Contributions: B.N. and D.C. conceived and designed the research. F.L. fabricated titanium alloy specimens by EBM and characterized material defects. Q.L. and B.L. performed the fatigue test. S.L. and H.Q. analyzed experimental data. Q.L. and B.S. wrote the manuscript. All authors have read and agreed to the published version of the manuscript.

Funding: This research was funded by the R & D plan for key areas in Guangdong Province (2020B010186001), the Science and Technology Program of the Ministry of Science and Technology (G2022030060L), the Science and Technology Project in Guangdong (2020b15120093, 2020B121202002), the Overseas Famous Teacher Project of Guangdong (BGK46303), the R & D plan for key areas in Jiangxi Province (20201BBE51009, 20212BBE51012), and the Science and Technology Research Project of Foshan (2220001005305).

Data Availability Statement: The data presented in this study are available upon request from the corresponding author.

Conflicts of Interest: The authors declare no conflict of interest.

References

1. Zhao, Q.; Sun, Q.; Xin, S.; Chen, Y.; Wu, C.; Wang, H.; Xu, J.; Wan, M.; Zeng, W.; Zhao, Y. High-strength titanium alloys for aerospace engineering applications: A review on melting-forging process. *Mater. Sci. Eng. A* **2022**, *845*, 143260. [CrossRef]
2. Zhang, Y.; Zhang, H.; Xue, J.; Jia, Q.; Wu, Y.; Li, F.; Guo, W. Microstructure transformed by heat treatment to improve fatigue property of laser solid formed Ti6Al4V titanium alloy. *Mater. Sci. Eng. A* **2023**, *865*, 144363. [CrossRef]
3. Tran, T.Q.; Chinnappan, A.; Lee, J.K.Y.; Loc, N.H.; Tran, L.T.; Wang, G.; Kumar, V.V.; Jayathilaka, W.A.D.M.; Ji, D.; Doddamani, M.; et al. 3D printing of highly pure copper. *Metals* **2019**, *9*, 756. [CrossRef]
4. Wang, J.; Pan, Z.; Wang, Y.; Wang, L.; Su, L.; Cuiuri, D.; Zhao, Y.; Li, H. Evolution of crystallographic orientation, precipitation, phase transformation and mechanical properties realized by enhancing deposition current for dual-wire arc additive manufactured Ni-rich NiTi alloy. *Addit. Manuf.* **2020**, *34*, 101240. [CrossRef]
5. Galarraga, H.; Warren, R.; Lados, D.; Dehoff, R.; Kirka, M.; Nandwana, P. Effects of heat treatments on microstructure and properties of Ti-6Al-4V ELI alloy fabricated by electron beam melting (EBM). *Mater. Sci. Eng. A* **2017**, *685*, 417–428. [CrossRef]
6. Gao, T.; Xue, H.; Sun, Z.; Retraint, D.; He, Y. Micromechanisms of crack initiation of a Ti-8Al-1Mo-1V alloy in the very high cycle fatigue regime. *Int. J. Fatigue* **2021**, *150*, 106314. [CrossRef]
7. Liu, F.; Peng, H.; Liu, Y.; Wang, C.; Wang, Q.; Chen, Y. Crack initiation mechanism of titanium alloy in very high cycle fatigue regime at 400 °C considering stress ratio effect. *Int. J. Fatigue* **2022**, *163*, 107012. [CrossRef]
8. Hrabe, N.; Gnäupel-Herold, T.; Quinn, T. Fatigue properties of a titanium alloy (Ti–6Al–4V) fabricated via electron beam melting (EBM): Effects of internal defects and residual stress. *Int. J. Fatigue* **2017**, *94*, 202–210. [CrossRef]
9. Chern, A.; Nandwana, P.; Yuan, T.; Kirka, M.; Dehoff, R.; Liaw, P.; Duty, C. A review on the fatigue behavior of Ti-6Al-4V fabricated by electron beam melting additive manufacturing. *Int. J. Fatigue* **2019**, *119*, 173–184. [CrossRef]

10. Romano, S.; Brückner-Foit, A.; Brandão, A.; Gumpinger, J.; Ghidini, T.; Beretta, S. Fatigue properties of AlSi10Mg obtained by additive manufacturing: Defect-based modelling and prediction of fatigue strength. *Eng. Fract. Mech.* **2018**, *187*, 165–189. [CrossRef]
11. Niu, X.; Zhu, S.P.; He, J.C.; Liao, D.; Correia, J.A.; Berto, F.; Wang, Q. Defect tolerant fatigue assessment of AM materials: Size effect and probabilistic prospects. *Int. J. Fatigue* **2022**, *160*, 106884. [CrossRef]
12. He, J.C.; Zhu, S.P.; Luo, C.; Niu, X.; Wang, Q. Size effect in fatigue modelling of defective materials: Application of the calibrated weakest-link theory. *Int. J. Fatigue* **2022**, *165*, 107213. [CrossRef]
13. Li, H.; Tian, Z.; Zheng, J.; Huang, K.; Nie, B.; Xu, W.; Zhao, Z. A defect-based fatigue life estimation method for laser additive manufactured Ti-6Al-4V alloy at elevated temperature in very high cycle regime. *Int. J. Fatigue* **2023**, *167*, 107375. [CrossRef]
14. Günther, J.; Krewerth, D.; Lippmann, T.; Leuders, S.; Tröster, T.; Weidner, A.; Biermann, H.; Niendorf, T. Fatigue life of additively manufactured Ti–6Al–4V in the very high cycle fatigue regime. *Int. J. Fatigue* **2017**, *94*, 236–245. [CrossRef]
15. Jiang, Q.; Li, S.; Zhou, C.; Zhang, B.; Zhang, Y. Effects of laser shock peening on the ultra-high cycle fatigue performance of additively manufactured Ti6Al4V alloy. *Opt. Laser Technol.* **2021**, *144*, 107391. [CrossRef]
16. Du, L.; Qian, G.; Zheng, L.; Hong, Y. Influence of processing parameters of selective laser melting on high-cycle and very-high-cycle fatigue behaviour of Ti-6Al-4V. *Fatigue Fract. Eng. Mater. Struct.* **2021**, *44*, 240–256. [CrossRef]
17. Qian, G.; Li, Y.; Paolino, D.; Tridello, A.; Berto, F.; Hong, Y. Very-high-cycle fatigue behavior of Ti-6Al-4V manufactured by selective laser melting: Effect of build orientation. *Int. J. Fatigue* **2020**, *136*, 105628. [CrossRef]
18. Chi, W.; Wang, W.; Li, Y.; Xu, W.; Sun, C. Defect induced cracking and modeling of fatigue strength for an additively manufactured Ti-6Al-4V alloy in very high cycle fatigue regime. *Theor. Appl. Fract. Mec.* **2022**, *119*, 103380. [CrossRef]
19. Shui, X.; Yamanaka, K.; Mori, M.; Nagata, Y.; Kurita, K.; Chiba, A. Effects of post-processing on cyclic fatigue response of a titanium alloy additively manufactured by electron beam melting. *Mater. Sci. Eng. A* **2017**, *680*, 239–248. [CrossRef]
20. Sun, C.; Chi, W.; Wang, W.; Duan, Y. Characteristic and mechanism of crack initiation and early growth of an additively manufactured Ti-6Al-4V in very high cycle fatigue regime. *Int. J. Mech. Sci.* **2021**, *205*, 106591. [CrossRef]
21. Caivano, R.; Tridello, A.; Chiandussi, G.; Qian, G.; Paolino, D.; Berto, F. Very high cycle fatigue (VHCF) response of additively manufactured materials: A review. *Fatigue Fract. Eng. Mater. Struct.* **2021**, *44*, 2919–2943. [CrossRef]
22. Nie, B.; Liu, S.; Wu, Y.; Song, Y.; Qi, H.; Shi, B.; Zhao, Z.; Chen, D. Very High Cycle Fatigue Damage of TC21 titanium alloy under high/low two-step stress loading. *Crystals* **2023**, *13*, 139. [CrossRef]
23. Yang, K.; He, C.; Huang, Q. Very high cycle fatigue behaviors of a turbine engine blade alloy at various stress ratios. *Int. J. Fatigue* **2017**, *99*, 35–43. [CrossRef]
24. Bathias, C. Piezoelectric fatigue testing machines and devices. *Int. J. Fatigue* **2006**, *28*, 1438–1445. [CrossRef]
25. Nie, B.; Zhao, Z.; Chen, D.; Liu, S.; Lu, M.; Zhang, J.; Liang, F. Effect of basketweave microstructure on very high cycle fatigue behavior of TC21 titanium alloy. *Metals* **2018**, *8*, 401. [CrossRef]
26. Nie, B.; Zhao, Z.; Liu, S.; Chen, D.; Ouyang, Y.; Hu, Z.; Fan, T.; Sun, H. Very high cycle fatigue behavior of a directionally solidified Ni-base superalloy DZ4. *Materials* **2018**, *11*, 98. [CrossRef]
27. Zhao, A.; Xie, J.; Sun, C.; Lei, Z.; Hong, Y. Prediction of threshold value for FGA formation. *Mater. Sci. Eng. A* **2011**, *528*, 6872–6877. [CrossRef]
28. Hong, Y.; Liu, X.; Lei, Z.; Sun, C. The formation mechanism of characteristic region at crack initiation for very-high-cycle fatigue of high-strength steels. *Int. J. Fatigue* **2016**, *89*, 108–118. [CrossRef]
29. Zhang, H.; Yu, F.; Li, S.; He, E. Fine granular area formation by damage-induced shear strain localization in very-high-cycle fatigue. *Fatigue Fract. Eng. Mater. Struct.* **2021**, *44*, 2489–2502. [CrossRef]
30. Chai, G.; Zhou, N.; Ciurea, S.; Andersson, M.; Peng, R. Local plasticity exhaustion in a very high cycle fatigue regime. *Scr. Mater.* **2012**, *66*, 769–772. [CrossRef]
31. Du, L.; Pan, X.; Qian, G.; Zheng, L.; Hong, Y. Crack initiation mechanisms under two stress ratios up to very-high-cycle fatigue regime for a selective laser melted Ti-6Al-4V. *Int. J. Fatigue* **2021**, *149*, 106294. [CrossRef]